Performance Tradeoffs Posed by Moving Magnet Actuators in Flexure-Based Nanopositioning

David B. Hiemstra, Gaurav Parmar, and Shorya Awtar

***Abstract*—Moving magnet actuators (MMAs) are direct-drive, single-phase electromagnetic linear actuators that provide frictionless and backlash-free motion over a range of several millimeters. This paper investigates the feasibility of using MMAs to simultaneously achieve large range, high speed, and high motion quality in flexure-based nanopositioning systems. Component and system level design challenges and associated tradeoffs in meeting the aforementioned nanopositioning performance are discussed and derived. In particular, it is shown that even as the overall size of a traditional MMA is varied, the actuation force remains directly proportional to the square root of the actuator's moving magnet mass and the square root of power consumed. This proportionality constant, identified as the *dynamic actuator constant*, serves as a figure of merit for MMAs. When an MMA is employed in a flexure-based nanopositioning system, this constant directly impacts the system-level positioning performance in terms of range, resolution, speed, and temperature rise. This quantitative determination highlights the significance of incorporating a thermal management system for heat dissipation, minimizing noise and harmonic distortion in the current driver, and improving the force–stroke uniformity of the actuator. Based on this understanding, a single-axis nanopositioning system, which simultaneously achieves 10 mm range, 4 nm resolution, open-loop natural frequency of 25 Hz, and temperature rise of less than 0.5 °C, is designed, fabricated, and tested. Preliminary controller design and closed-loop operation highlight the potential and limitations of MMAs in large-range, high-speed nanopositioning.**

***Index Terms*—Dynamic actuator constant, moving magnet actuator (MMA), nanopositioning, performance tradeoffs, thermal management.**

I. Introduction and Motivation

A MOVING magnet actuator (MMA) is a direct-drive, single-phase, linear electromagnetic actuator. MMAs provide noncontact, frictionless, and cogging-free actuation over a range of motion of several millimeters, which makes them useful in applications such as precision motion systems [1], disk drives [2], and automotive valves [3]. A traditional MMA architecture is shown in Fig. 1, where an axially oriented cylindrical permanent magnet sandwiched between two iron pole pieces forms the mover. The stator consists of a back iron along with two oppositely wound coils connected in series. The permanent magnet's field produces a Lorentz force on the mover, proportional to the coil current.

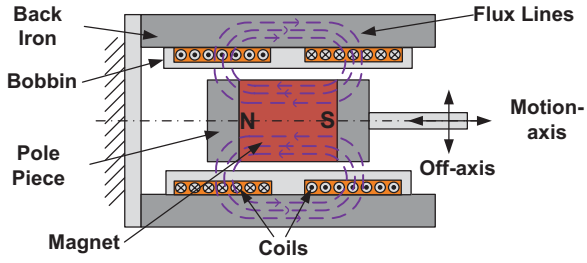

Fig. 1. Schematic of a traditional MMA.

The goal of this paper is to systematically investigate the feasibility of MMAs in enabling large range (∼10 mm) and high scanning speed (>10 Hz or 300 mm/s) in flexure-based nanopositioning systems. A nanopositioning system is a macroscale motion system that is capable of nanometric (<10 nm) precision (repeatability of motion), accuracy (lack of error in motion), and resolution (minimum incremental motion) [4]. Because of this high *motion quality*, nanopositioning systems are employed in various sensitive applications to provide relative scanning motion. These include scanning probe microscopy [5], [6], scanning probe lithography [7], nanometrology [7], and hard-drive and semiconductor inspection [8]. However, one of the main drawbacks of existing nanopositioning systems is their relatively small motion range of a few hundred microns per axis [9]. Increasing this range to several millimeters will significantly increase the "area-coverage" in scanning nanometrology and direct-write nanomanufacturing, potentially leading to large-scale industrial applications of these techniques. In addition to nanometric motion quality and large range, high scanning speed is also desirable to maximize throughput. Furthermore, minimizing and expediently removing any heat generated from the motion system is also important because of the highly sensitive nature of these applications [10]–[12].

A nanopositioning system generally comprises a bearing for motion guidance, actuator(s), sensor(s), driver(s), and control logic and hardware. Closed-loop operation is necessary to achieve nanometric motion quality over the desired frequency range [13]. There are several fundamental challenges in simultaneously achieving large motion range, high motion quality, and high speed in nanopositioning systems [4]. These arise from limitations of the individual components, their mechanical integration and physical interaction, and the closed-loop operation of the overall motion system.

Manuscript received February 9, 2012; revised July 11, 2012 and September 11, 2012; accepted October 7, 2012. Recommended by Technical Editor Y. Sun. This work was supported in part by the National Science Foundation under Grant CMMI 1100807. The work of G. Parmar was supported by a Measurement Science and Engineering Fellowship from the National Institute of Science and Technology. The first two authors have contributed equally to this work.

The authors are with the Department of Mechanical Engineering, University of Michigan, Ann Arbor, MI 48105 USA (e-mail: davidbh@umich.edu; parmar@umich.edu; awtar@umich.edu).

Color versions of one or more of the figures in this paper are available online at http://ieeexplore.ieee.org.

Digital Object Identifier 10.1109/TMECH.2012.2226738

Nanopositioning systems predominantly employ noncontact bearings to avoid friction and backlash [4]. In general, the nonlinear and parameter-varying characteristics of friction, which are difficult to model, restrict the achievable motion quality [14], [15]. While advanced design and control methods have demonstrated steady-state nanometric precision and resolution in point-to-point positioning [16]–[18], tracking dynamic command profiles that involve frequent direction reversal is still an unmet challenge [19]. Although magnetic and aerostatic bearings are promising options for nanopositioning, this paper focuses on flexure bearings because of their design simplicity, zero maintenance, potentially infinite life, compact size, low cost, and ability to provide the desired motion range [4].

Also, there exist several sensing options that are capable of the desired range, speed, precision, and resolution [20]. One of these—a linear optical encoder—is used in this study.

One of the major pending challenges in achieving large-range high-speed nanopositioning is that of actuation technology, which constitutes the focus of this paper. Several existing actuator options along with their limitations are discussed in Section II. The potential of MMAs is highlighted in comparison to these actuators. In Section III, inherent tradeoffs in the specifications of an MMA and their impact on the performance of flexure-based nanopositioning systems are qualitatively discussed. A systematic model for the MMA is used to derive a new figure of merit that captures the dynamic performance of the actuator. Next, performance tradeoffs at the motion system level are quantitatively identified in terms of the individual specifications of the actuator, actuator driver, flexure bearing, and thermal management system (TMS). In Section IV, this understanding is employed in the optimal design and fabrication of a single-axis nanopositioning system comprising the aforementioned four components. Preliminary testing results for the individual components as well as the overall nanopositioning system are reported in Section V. Motion range of 10 mm, open-loop bandwidth of 25 Hz, and motion stage temperature rise less than 0.5 °C are experimentally demonstrated. A lead–lag controller is implemented to achieve 4 nm (RMS) steady-state precision and resolution in point-to-point positioning experiments over this motion range. Section VI provides a summary of contributions, open questions, and future work.

II. Actuators Used in Nanopositioning

The performance of an actuator is usually specified by its motion range, resolution capability, output force, speed of response, size, power consumption, efficiency, etc. [20], [21]. In general, it is difficult to simultaneously achieve desirable values of all these specifications due to limitations and tradeoffs arising from the construction and underlying physics of the actuator [22].

A. Piezoelectric Stack Actuators

Given their high resolution, force, operating bandwidth, and lack of friction and backlash, piezoelectric actuators based on lead zirconate titanate (PZT) are the standard actuation method used in most existing nanopositioning systems. The primary limitation of these actuators is their inherently small stroke ($\sim$10–200 μm) [4], [13]. In an attempt to overcome this, PZT actuators may be integrated with suitable flexure-based motion transmissions that amplify their range [23]–[25]. However, amplifying the motion by N times reduces the actuator's effective stiffness by N^2 times and force by N times, at the output of the transmission. This leads to a smaller than expected stroke when the actuator and amplifier are integrated with a flexure bearing because of the blocking force that the latter generates. In many instances, the transmission may be cleverly designed such that it also serves as the flexure bearing and provides motion guidance for the motion system [23]. In these cases, the stroke of the motion system is indeed amplified to be N times that of the actuator, but the natural frequency of the motion system scales inversely with N. Furthermore, to achieve high transmission ratios and yet maintain an overall compact motion system footprint, these designs exploit kinematic nonlinearities in the transmission mechanism. However, this produces a transmission ratio that changes considerably, especially over a large motion range, as well as the possibility of overconstraint [24]. Moreover, the elastic deviation of a flexure-based transmission from true kinematic characteristics leads to "lost motion" between the actuator and motion stage [25].

B. Quasi-Static and Ultrasonic Piezomotors

These motors employ a repetitive actuation pattern that converts the limited displacement of a piezoceramic element to theoretically infinite displacement. The actuation pattern relies on friction to produce relative motion between the piezoceramic element and the mover. Quasi-static piezomotors, which implement this repetition at frequencies lower than the resonant frequency of their piezoceramic element, operate on either the *clamping principle* or the *inertial principle*. In the former case, motion is generated through a succession of quasi-static coordinated clamp/unclamp and extension/contraction *step* cycles. These so-called inchworm motors typically have a step size in the range of 10 nm to 1 μm and operating speed less than 10 mm/s [13], [21]. In the inertial style quasi-static piezomotors, inertia and the difference in dynamic and static friction are exploited to produce discrete "slipping" steps, which may be repeated indefinitely [26]. While these quasi-static piezomotors provide good performance in large-range point-to-point positioning with nanometric precision, they are not suitable for high-speed scanning where precision has to be maintained along the entire motion profile. This is because of the impact-induced axial vibrations during steps, often termed as "glitch," which is typically of the order of 50 nm [13], [26]. These glitches become even more prominent at higher speeds.

Ultrasonic piezomotors excite resonant bending modes of a piezoceramic element in the ultrasonic frequency range which combine to produce a repeating elliptical stepping motion. These actuators provide higher speeds (100–500 mm/s) but much lower force capability ($<$10 N) [21], [27]. Another potential drawback of ultrasonic actuators is heat generation [27]. Furthermore, a major drawback of all quasi-static and ultrasonic piezomotors, especially for large-range nanopositioning, is their low fatigue life [13].

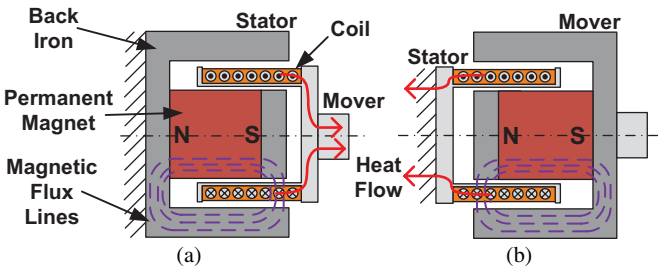

Fig. 2. VCA schematic with (a) coil as mover and (b) magnet as mover.

C. Linear Electromagnetic Actuators

Recognizing the limitations of piezoelectric actuators, several direct-drive, linear electromagnetic actuators have been designed and investigated for large-range, high-speed nanopositioning [1], [4], [28]–[34]. Although multi-phase electromagnetic linear motors provide noncontact operation over a large motion range (∼100 mm), they sometimes suffer from cogging, thus limiting the achievable precision [11], [33]. While cogging may be eliminated via slot-less and iron-less constructions [35], the single-phase noncommuted voice coil actuator (VCA) and moving magnet actuator (MMA) offer unmatched simplicity in design and construction, along with noncontact cog-free motion, low cost, and sufficiently large stroke [4], [28], [30], [32].

A cross section of a typical VCA configuration is shown in Fig. 2(a), where an axially magnetized cylindrical permanent magnet and an integrated tubular back iron form the stator, and a coil wound on a bobbin forms the mover. The heavy permanent magnet and back iron are stationary, allowing the lightweight coil to achieve a fast mechanical response time [30], [31]. However, heat dissipation from the coil connected to the motion stage and disturbance due to the moving coil wires degrade the motion quality [36]. To overcome these problems, the voice coil is sometimes employed in an inverted configuration [4], [32] [see Fig. 2(b)]. While this configuration eliminates disturbance from moving wires and improves thermal dissipation, it adds the large mass of the magnet and back iron to the motion stage. When employed with a flexure bearing, the resulting low natural frequency not only limits the open-loop and closed-loop bandwidth of the overall motion system but also compromises closed-loop disturbance rejection, which is necessary to achieve nanometric motion quality [37].

The MMA shown in Fig. 1 embodies all the benefits of the inverted voice coil and also has a significantly lower moving mass since the relatively heavy back iron remains static along with the coil. Additionally, the disturbance due to the moving coil wires is eliminated. The static back iron also allows for improved heat dissipation and keeps the heat generated due to resistive losses in the coils further away from the motion stage. While these advantages make MMAs a promising candidate for actuation in nanopositioning, several design challenges and performance tradeoffs remain, as discussed next. While other variations exist [31], [38], the traditional MMA architecture in Fig. 1 is most commonly used because of its simple construction and practical viability, and is therefore the focus of this paper.

III. MMA Performance Tradeoffs and Design Challenges

The requirements placed by the desired nanopositioning performance on the MMA specifications are qualitatively discussed next.

1) In the absence of friction and backlash, the motion quality of the nanopositioning system is determined by its closed-loop tracking performance, which is primarily limited by noise and harmonic distortion in the electrical driver that supplies current to the actuator. Higher open-loop bandwidth helps attenuate the effect of this noise/distortion in closed-loop operation [37], enabling higher motion quality. The open-loop bandwidth, which correlates with the first natural frequency of the motion system, can be increased by increasing the flexure stiffness and decreasing the overall moving mass. The noise and distortion in the electrical driver can also be reduced at the source by lowering the actuator power input.
2) A large desired stroke and high flexure bearing stiffness demand a large actuation force. For high scanning speed and large stroke, the actuator also has to overcome inertial loads, which place further demands on the actuation force. For the scanning applications described earlier, external forces on the motion stage are negligible in comparison to the spring and inertial forces.
3) Nonuniformity in the MMA's force output over its stroke, for a fixed current input, also leads to nonlinearities that produce higher order harmonics in open-loop as well as closed-loop operation [11]. While the adverse effect of these harmonics on the motion quality may be mitigated by a large open-loop bandwidth and therefore better closed-loop disturbance rejection, the actuator can also be designed to provide greater force–stroke uniformity.
4) Temperature rise due to power dissipated as heat is detrimental to the components as well as the assembly of the motion system. The feedback sensor can lose accuracy and the mechanical assembly can develop undesired stresses and distortion. Minimizing these effects requires minimizing the power consumption of the actuator and removing the generated heat from the system, even though the heat source in an MMA is located further away from the motion stage as compared to a VCA.
5) Separation of the back iron from the permanent magnet in an MMA introduces the risk of snap-in instability in the direction perpendicular to the motion axis [39]. This instability gets worse with increasing actuator force, and can be mitigated by a flexure bearing that provides a higher positive off-axis stiffness compared to the negative off-axis stiffness associated with the actuator.

This discussion reveals several conflicting requirements placed on the MMA specifications—force capability, force–stroke uniformity, moving mass, power consumed, heat generated, etc. For example, the force output of an MMA can be raised by increasing either the moving magnet mass or the input power, but both are undesirable for reasons explained previously. Reducing the flexure stiffness in the motion direction allows a

larger portion of the actuation force to be devoted to inertial loads, leading to higher operating speeds, but lower stiffness also reduces the open-loop bandwidth and compromises disturbance rejection capability. While greater force–stroke uniformity reduces the reliance on large open-loop bandwidth to provide the desired motion quality, it typically requires an axially longer coil, which in turn implies greater power consumption and heat generation. Furthermore, any design features that increase the actuation force also increase the negative off-axis stiffness associated with the MMA. Clearly, these design challenges and performance tradeoffs cut across the multiple components and physical domains of the overall motion system.

Although such tradeoffs associated with MMAs have been previously identified, the discussion has been largely component-level and qualitative [31], [38], [40]. This paper attempts to systematically capture these design limitations and performance tradeoffs in a model-based quantitative manner, so as to identify the key bottlenecks to better system-level performance. For the MMA, it is important to identify good figures of merit that capture the aforementioned specifications and tradeoffs quantitatively. Figures of merit help compare MMAs from different vendors, determine the suitability of an MMA for a given application, and set the objective in the conception and optimization of new MMA designs. It is also important to recognize if there exist fundamental limits on these figures of merit, arising from the inherent construction and underlying physics of the actuator. One such figure of merit that has been traditionally used is the *actuator constant*, which is defined as the actuator output force per unit square root of power consumed. It captures the actuator-level tradeoff that the output force of an MMA cannot be indefinitely increased without increasing the power input and heat generated. However, this actuator constant only captures the quasi-static performance of the MMA since it does not incorporate the actuator's moving mass. As a result, it does not reflect on the dynamic performance of the MMA when used in a flexure-based nanopositioning system. Other figures of merit for MMAs that do capture some degree of dynamic performance include the *electrical time constant* and the *mechanical time constant*. The electrical time constant τ_e is defined as the rise time of the current for a step voltage change and depends on the inductance to resistance ratio of the coil. While it does represent a tradeoff between the current rise time and heat generation, this tradeoff is readily overcome via the use of a current driver. The mechanical time constant τ_m is defined as the rise time of the velocity for a step voltage change and depends on the actuator constant as well as the moving mass. However, it does not reveal any inherent tradeoff associated with the construction and physics of the MMA.

A. MMA Figure of Merit to Capture Dynamic Performance

In order to capture dynamic performance, an MMA figure of merit is needed that not only includes the continuous output force and the power consumption, but also includes the actuator's moving mass. To quantitatively investigate the existence of such a figure of merit, the effect of geometric scaling on the actuator output force, power consumption, and moving mass is considered. Fig. 3 shows a lumped parameter model of an MMA with a traditional architecture. The dimensions l_m, l_p, r_m, and t_a denote the nominal magnet axial length, pole piece length, magnet radius, and magnetic air gap radial thickness, respectively. α is the geometric scaling factor. The following assumptions are made to simplify the analysis. 1) Any fringing and leakage flux is neglected. 2) The permeability of the back iron and the pole pieces is much larger than that of vacuum ($\mu_{\text{iron}} \gg \mu_0$). Hence, the reluctances of the back iron and the pole pieces are neglected. 3) The permeability of the magnet, aluminum, and air is approximately equal to that of vacuum ($\mu_{\text{air}} \approx \mu_{\text{Al}} \approx \mu_{\text{magnet}} \approx \mu_0$). 4) All the radial space between the pole pieces and the back iron t_a is occupied by coils. In other words, the mechanical air gap t_g is negligible compared the thickness of coil t_c.

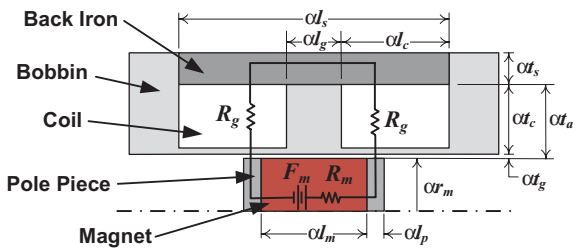

Fig. 3. MMA geometry and simplified lumped parameter model.

Based on standard lumped parameter magnetostatic analysis [41], the magnetomotive force (F_m) and the lumped reluctances of the magnet and the air gap (R_m and R_g) are given by

$$F_m = \frac{\alpha B_r l_m}{\mu_m} \quad R_m = \frac{l_m}{\pi \alpha \mu_m r_m^2} \quad R_g = \frac{\ln\left(1 + t_a/r_m\right)}{2\pi\alpha\mu_0 l_p} \tag{1}$$

where B_r is the remanent flux density of the permanent magnet, and μ_m and μ_o are the permeability values for the permanent magnet and vacuum, respectively. Next, the resultant flux ϕ and average magnetic flux density in the air gap B_g are given by

$$\phi = \frac{F_m}{R_m + 2R_g} \quad B_g = \frac{\phi}{2\pi\alpha^2\left(r_m + t_a/2\right) l_p}. \tag{2}$$

The force output F and power consumed, i.e., dissipated as heat P, and the moving mass m_a, can be determined to be

$$\begin{aligned} F &= B_g i l_w = i\phi \frac{2\alpha t_a}{d^2} \\ P &= i^2 R = i^2 \frac{\rho_c l_w}{A_w} = i^2 \rho_c \frac{16\alpha^3 l_p t_a \left(r_m + t_a/2\right)}{d^4} \\ m_a &= \rho_m \pi \alpha^3 r_m^2 l_m \end{aligned} \tag{3}$$

where i is the coil current, R is the coil resistance, ρ_c is the resistivity of the coil wire, d is the wire diameter, A_w is the cross-sectional area of the wire, l_w is the total length of the wire in the air gap, and ρ_m is the mass density of the magnet. It should be noted that the current i, force F, and power P are all

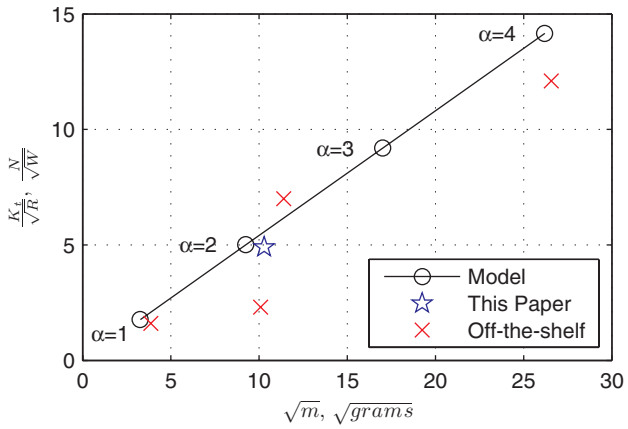

Fig. 4. Effect of geometric scaling on MMA performance.

dynamic variables. The relations given in (3) lead to

$$\frac{F}{\sqrt{P}\sqrt{m_a}} = \frac{B_r}{\left(\frac{l_m\, l_p}{r_m^2} + \ln\left(1+\frac{t_a}{r_m}\right)\right)}\sqrt{\frac{\pi l_m\, l_p\, t_a}{4\rho_c \rho_m\, r_m^2\,(r_m + t_a/2)}}. \tag{4}$$

In the aforementioned relation, the scaling factor α, wire diameter d, and coil current i get canceled out, and the left-hand side term is found to be dependent on only the physical constants and nominal dimensions, which are constant for a given MMA architecture. This shows that the force output F remains directly proportional to the square root of the actuator moving mass m_a and the square root of power consumed P, irrespective of the scale of the actuator α. Equation (4) may be restated as follows:

$$\frac{F}{\sqrt{P}\sqrt{m_a}} = \frac{K_t}{\sqrt{R}\sqrt{m_a}} = \beta \text{ (constant)} \tag{5}$$

where K_t is the force constant (force per unit current) of the MMA. The constant β (units of $\sqrt{\text{Hz}}$), therefore, turns out be an important figure of merit in the design of an MMA, and is referred to, hereafter, as the *dynamic actuator constant*. While this constant is related to the mechanical time constant ($\tau_m = 1/\beta^2$), it provides important design insight that the latter does not. It reveals an inherent tradeoff associated with the force, moving mass, and the power consumption of an MMA, which cannot be overcome by varying the actuator size. It should be noted, however, that β varies when the relative proportions between the actuator's dimensions are changed.

While several simplifying assumptions were made in the derivation of the dynamic actuator constant, relation (5) is found to be true even when these assumptions are removed in a finite element analysis (FEA) using Maxwell. This is shown in Fig. 4. The ratio $(K_t/\sqrt{R})$, which is the actuator constant, is plotted against the square root of the actuator moving mass $(\sqrt{m_a})$ for different values of the scaling factor α. The slope of the curve represents the dynamic actuator constant ($\beta = 14$), for the particular choice of actuator dimension proportions.

In addition to the aforementioned closed-form and finite elements analysis, a survey of commercially available off-the-shelf MMAs [42]–[45] further validates the significance of relation (5). All these MMAs are of the traditional architecture, offer a motion range of around 10 mm, and are of various sizes and proportions. However, as seen in Fig. 4, they all lie close to the straight line corresponding to $\beta = 14$. This suggests that the dynamic actuator constant, in addition to being independent of the actuator size, cannot be increased beyond a certain limit even by optimizing the dimensional proportions.

B. Impact of β on the Motion System Performance

When the MMA is employed in a flexure-based nanopositioning system, an important consequence of relation (5) is that it places a fundamental limit on the system open-loop bandwidth (ω_n), desired scanning speed (ω), desired motion range ($\pm\Delta_o$), power consumed (P), and the moving masses (actuator m_a, motion stage m). Assuming a sinusoidal motion profile ($\Delta = \Delta_o \cos\omega t$), this limit may be derived by equating the actuation force with the spring and inertial forces

$$F = K_t i = (m + m_a)\,\left|\omega_n^2 - \omega^2\right|\Delta \tag{6}$$

where $\omega_n^2 = K_y/(m + m_a)$ and K_y is the flexure stiffness.

This indicates that when the desired scanning speed is less than the natural frequency of the system ($\omega \ll \omega_n$), the required actuation force is dominated by the spring stiffness, and the actual scanning speed is less important. However, when the scanning speed is greater than the natural frequency ($\omega \gg \omega_n$), the required actuation force is dominated by inertial loads and depends on the square of the scanning speed. These two conditions represent the worst case actuation force requirements. As expected, the actuation force becomes very small around resonance ($\omega \approx \omega_n$).

Substituting β from (5) and $P = i^2 R$ in (6), the minimum required actuation force may be restated as

$$\beta \cdot \frac{\sqrt{m_a}}{m + m_a} \geq \Delta \cdot \left|\omega_n^2 - \omega^2\right| \cdot \frac{1}{\sqrt{P}}. \tag{7}$$

This expression quantitatively captures the performance tradeoff that achieving large motion range, high resolution (enabled by good disturbance rejection due to high natural frequency), high scanning speed, and low power consumption (to minimize temperature rise and driver noise/distortion) are all at odds with respect to each other. The only way to simultaneously achieve these nanopositioning performance attributes is to use an MMA that provides a large β and minimize all moving masses in the system.

This represents a system level performance tradeoff. If, for example, the flexure bearing is designed to be stiffer to increase the open-loop bandwidth and improve disturbance rejection of the driver noise/distortion and actuator force–stroke nonuniformity, it would also require an increase in the actuation force in order to retain the same motion range. But, as per the MMA tradeoff given by relation (5), this can only be achieved by increasing the magnet mass, for a given power consumption limit. Ultimately, using a stiffer bearing will not lead to the desired increase in the open-loop bandwidth. Trying to improve disturbance rejection via controller design hurts the closed-loop system stability robustness [37]. Therefore, it becomes important to employ an electrical driver with minimal noise and distortion, and design

the MMA with maximal force–stroke uniformity. Furthermore, while increasing the current and therefore power into the system will improve its overall performance, it will also produce a temperature rise that is detrimental. Therefore, any increase in power has to be matched by a TMS that carries the heat out of the system to maintain its temperature.

IV. Design and Fabrication of the Experimental Setup

In order to experimentally establish the validity of the dynamic actuator constant as an MMA figure of merit and to verify the performance limitations that it imposes on the overall motion system, a single-axis flexure-based nanopositioning system was designed, fabricated, and tested. This system comprises an MMA, an electrical driver, a symmetric double parallelogram flexure bearing, a novel TMS, a linear optical encoder, and feedback control hardware. The targeted positioning performance was set at range ± 5 mm, sinusoidal scanning speed 10 Hz, motion precision and resolution <5 nm, and temperature rise $<0.5\,^{\circ}$C. A high open-loop bandwidth was sought to reject disturbances and achieve the desired motion quality. At the same time, noise and harmonic distortion were minimized at the source in the electrical driver.

A custom-made driver, based on the MP111 power-OpAmp from Cirrus Logic, was designed and tested to achieve high signal-to-noise ratio (110 dB) and low total harmonic distortion (90 dB) [46]. This driver was operated in the current mode with a gain of 1 A/V to provide direct control of the actuation force over a 1 kHz bandwidth. This driver is rated for 20 W power; higher power tends to further increase the noise and harmonic distortion. Therefore, 20 W was set as the upper limit of power input to the MMA. Since, in the worst case scenario of steady-state operation, this input power is entirely converted to heat, the TMS was also designed to dissipate 20 W while maintaining the temperature of the motion stage within the targeted range.

A. MMA

The MMA dimensions and material were selected in a systematic manner to maximize β, while maintaining high force–stroke uniformity. In a minor deviation from the topology of Fig. 3, the designed MMA does not feature pole pieces. It can be separately shown that although removing the pole pieces reduces the force constant K_t, it leads to an overall higher value of β due to the reduced moving mass. All results presented in this section are based on FEA using Maxwell.

1) The minimum magnet length l_m is governed by the desired stroke Δ_o and the coil separation

$$l_m \geq 2\Delta_o + l_g. \tag{8}$$

The coil separation l_g should be large enough so that the fringing flux from one face of the magnet does not pass through the opposite coil when the magnet is at the end of the stroke. Otherwise, this would lead to reduced force–stroke uniformity. For a desired stroke of ± 5 mm and a chosen minimum coil separation of 10 mm, the magnet length was, therefore, selected to be 25.4 mm. The magnet dimension was also influenced by the standard available sizes.

2) While β is invariant with geometric scaling, it does vary with the dimensional proportions of the actuator. Therefore, once the magnet length is chosen, the magnet radius r_m and the coil thickness t_c can be selected to maximize β. Fig. 5(a) shows the effect of varying the magnet radius and coil thickness on β for a fixed coil length l_c. Based on this plot, and taking manufacturing constraints and standard magnet sizes into account, r_m and t_c were chosen to be 12.7 and 15 mm, respectively. Assuming neodymium–iron–boron (NdFeB) magnets, the actuator moving mass for these dimensions is 106 g. These selections lead to a β value of 14 $\sqrt{\text{Hz}}$ and an actuator constant of 4.5 N/$\sqrt{\text{W}}$, resulting in an achievable actuation force of 17 N for a power constraint of 20 W.

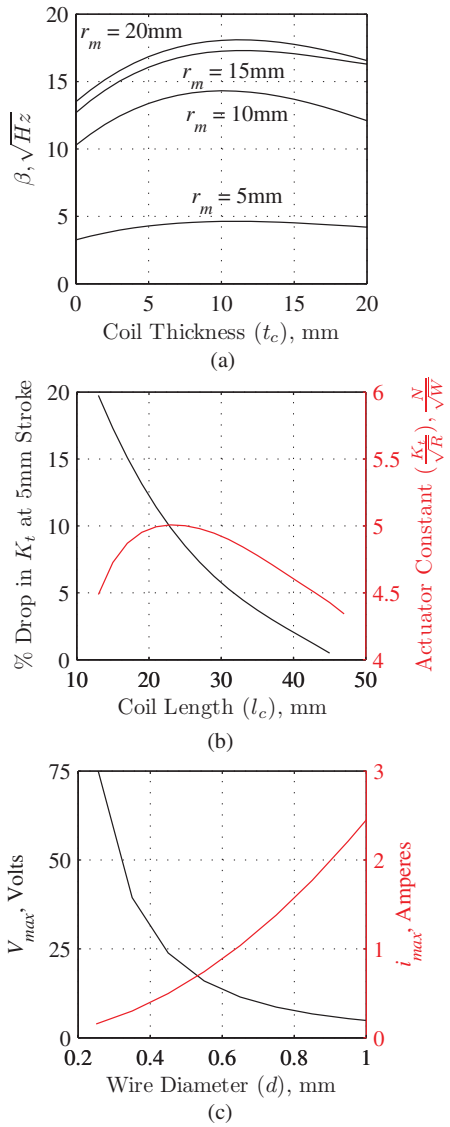

Fig. 5. MMA design tradesoffs. (a) Variation in the performance metric (β) with varying coil thickness and magnet radius. (b) Percentage drop in force constant at the ends of the stroke and actuator constant versus coil length. (c) Maximum continuous current and voltage requirement versus wire diameter.

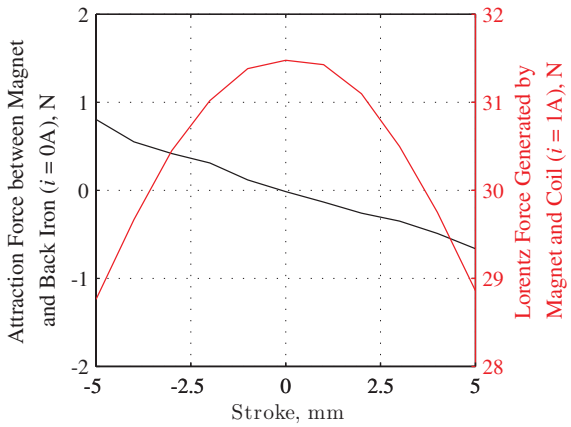

Fig. 6. Mover force versus stroke for $i = 0$ A and $i = 1$ A coil current.

3) With the assumption that the flux path width is approximately equal to the radius of the magnet, the coil length l_c is dictated by the stroke and the magnet radius as

$$l_c \geq 2\Delta_o + r_m > 22.7 \text{ mm}. \tag{9}$$

Increasing the length of the coil improves the force–stroke uniformity but only at the cost of an increase in the coil resistance, which reduces β. As shown in Fig. 5(b), the coil length was chosen to be 26 mm to limit the drop in force constant K_t at the ends of the stroke to be less than 10% without any appreciable loss in the dynamic actuator constant. The resultant Lorentz force on the moving magnet is plotted against its axial position for 1 A coil current in Fig. 6 confirming this force–stroke nonuniformity.

4) As shown previously in relation (4), β is only dependent on the volume of the coil and is independent of the wire diameter d. For example, although reducing d increases the coil resistance R, it also increases K_t due to greater number of turns, as per relation (3), thereby keeping β invariant. However, the choice of wire diameter presents a tradeoff between voltage and current, for a fixed power level of 20 W, as shown in Fig. 5(c). Using this plot, 25 AWG wire with a diameter of 0.455 mm was chosen to keep the required voltage below 25 V, a limit imposed by our power supply. This resulted in a maximum continuous current of 0.56 A and a coil resistance of 43.6 Ω.

5) The thickness of the back iron ($t_s = 7.6$ mm) is chosen such that the magnetic flux density in the iron remains below saturation for all values of coil current. Increasing the length of the back iron l_s reduces the axial magnetic force between the magnet and the back iron. This force, which acts in addition to the Lorentz force, tends to push the magnet toward the center of the stroke and is plotted explicitly in Fig. 6 for $i = 0$ A and $l_s = 65$ mm. It should be noted that while the Lorentz force component is symmetric with respect to zero stroke position, the overall force–stroke profile of the MMA turns out to be nonsymmetric due to the force between the magnet and the back iron. This latter force component is unique to MMAs and does not exist in VCAs, in which the magnet and back iron are rigidly attached.

TABLE I
MMA SPECIFICATIONS

Parameter	Value	Units
Dynamic actuator constant	14	$Hz^{1/2}$
Stroke	10	mm
Moving mass	106	g
Actuator constant	4.5	$NW^{-1/2}$
Force-stroke non-uniformity	9	%
Resistance	43.6	Ω
Inductance	2.6	mH
Radial / Axial size	36.8 / 85	mm
Air gap magnetic flux density	0.1 – 0.3	T

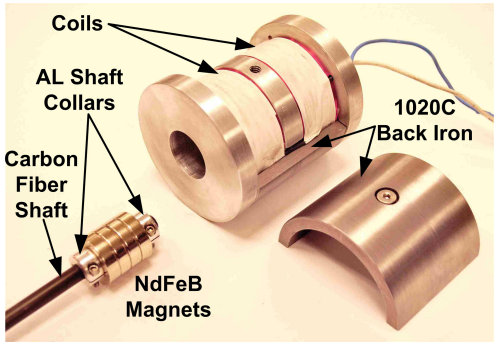

Fig. 7. MMA prototype.

Table I summarizes the MMA size and specifications. Based on this design, an MMA prototype was fabricated and assembled in-house, as shown in Fig. 7. The mover comprises a stack of four Grade 52 NdFeB axial magnets ($B_r = 1.45$ T) mounted on a lightweight carbon fiber shaft and constrained using aluminum shaft collars. One design constraint of this magnet is its maximum operating temperature of 80 °C, specified in the manufacturer's datasheet. Temperatures above this lead to a gradual reduction of the magnet's remanence. However, this risk is mitigated by the TMS described next. The coil bobbin was made of aluminum 6061 because of its good machinability and high thermal conductivity. Also, it serves as a shorted turn which reduces the effective coil inductance [47]. However, one drawback of using aluminum as bobbin material is its susceptibility to eddy currents, because of its high electrical conductivity. These eddy currents give rise to phase lag [48], thereby degrading the dynamic performance of the feedback loop. The physical air gap between the mover and bobbin was chosen to be 0.5 mm, primarily limited by manufacturing and assembly tolerances. The back iron was made from 1020C steel with a saturation flux density of 1.6 T. In order to simplify the assembly process, the back iron was designed as two symmetric halves so that the magnet and the bobbin can be easily assembled *a priori* without the iron being in the vicinity of the strong magnetic force generated by the permanent magnet.

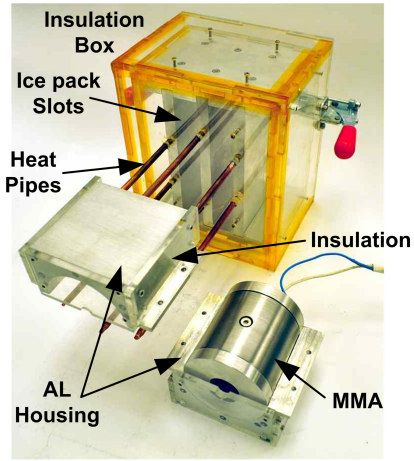

Fig. 8. TMS prototype.

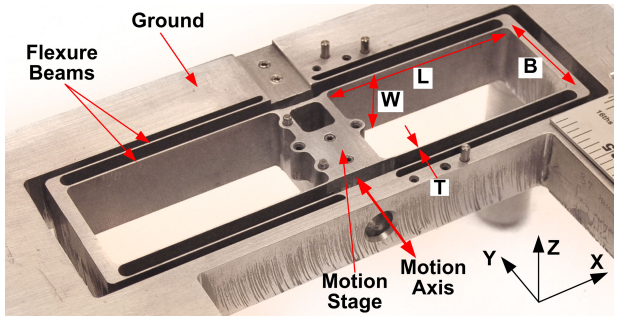

Fig. 9. Flexure bearing prototype.

B. TMS

During steady-state operation, which represents the worst case scenario of heat generation, most of the power sent to the actuator is converted to heat. As mentioned earlier, heat dissipated from the coils poses several potential problems. If 20 W of heat is not drawn away from the actuator coils, FEA and experimental results show that the temperature rise at the motion stage and the encoder scale is approximately 10 °C, and at the coil bobbin is more than 50 °C. Such a temperature rise, along with spatial thermal gradient, leads to significant internal stresses and distortion in the mechanical structure and assembly [11]. Also, a 10 °C temperature rise causes the 10 mm long Invar encoder scale (thermal expansion coefficient of 0.6 μm/m/°C) to expand by 60 nm. This loss in accuracy of the sensor cannot be compensated by using feedback control. All these factors adversely affect the precision and accuracy of the nanopositioning system. Furthermore, although the temperature rise is not large enough to damage the coils or the permanent magnet in the present case, overheating of these components should be generally avoided. Therefore, thermal management becomes a critical aspect of the overall system design.

In order to maintain the desired temperature stability, a novel passive TMS was designed and integrated with the MMA (see Fig. 8). While fan-based active heat dissipation systems can be designed to precisely control the temperature, they lead to air flow-induced vibrations that are detrimental to nanopositioning performance. Instead, we conceived a passive system that is based on latent heat transfer and therefore does not suffer from this disadvantage.

This TMS effectively transfers heat from the aluminum housing around the MMA coils to separately placed, water-sealed ice packs using wick-type copper heat pipes that serve as low thermal resistance paths. The heat generated at the coils is absorbed by ice as it converts to water, without any rise in its temperature. The aluminum housing and the racks containing ice packs are thermally insulated via a double-layered acrylic box in order to minimize any thermal fluctuations of the surrounding environment. The critical components of the TMS (heat pipes, ice packs, and aluminum racks) were designed using a lumped-parameter thermal model in order to ensure that the steady-state coil bobbin temperature remains near room temperature for at least 4 h of operation under constant 20 W power input to the actuator. Details of this model are provided in [49].

C. Flexure Bearing

A single-axis symmetric double-parallelogram flexure bearing, also known as the double-compound rectilinear spring mechanism [50], was designed and fabricated (see Fig. 9) to provide frictionless and backlash-free motion guidance over the entire range of motion. This design provides uniform motion direction stiffness over a relatively large stroke and high bearing stiffness in all other translation and rotation directions [51]. Aluminum 6061 was selected for the bearing material given its overall good flexure characteristics. As the first step, the size and mass of the motion stage were minimized ($m = 42$ g), while providing adequate space to interface the sensor and actuator. With the overall moving mass ($m+m_a$), dynamic actuator constant (β), power consumption limit (P), and desired stroke (Δ_o) and scanning speed (ω) all known, (7) predicts that the maximum achievable natural frequency (ω_n) is 27 Hz.

Accordingly, the beam thickness T, width W, length L, and spacing B in the flexure bearing were selected to be 0.75, 25.4, 80, and 40 mm, respectively. The resulting geometry provides a motion direction stiffness of 3.43 N/mm, stroke of ± 5 mm while maintaining a safety factor of 4 against yielding, and a natural frequency of 25 Hz.

The negative (destabilizing) stiffness of the off-axis force between the magnet and the back iron was calculated via electromagnetic FEA to be 1.3 N/mm at the nominal position. The stiffness values provided by the bearing in the X- and Z-directions are the lowest at the maximum motion stage displacement [51]. At the desired 5 mm displacement, these values are found to be 149.6 and 70.6 N/mm, respectively, thereby ensuring adequate off-axis stability of the magnet-back iron assembly.

D. Experimental Setup Assembly

In addition to the aforementioned subsystems, an off-the-shelf 5 nm, resolution linear optical encoder (RELM scale, Si-HN-4000 Read-head, and SIGNUM Interface from Renishaw) was used for position measurement of the motion stage. The assembly of the MMA, TMS, flexure bearing, and encoder is shown in

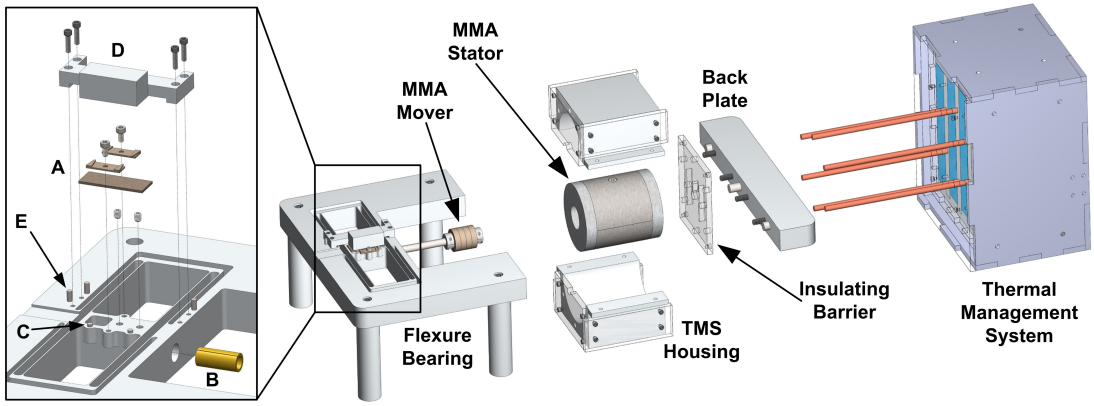

Fig. 10. Detailed CAD showing motion system assembly.

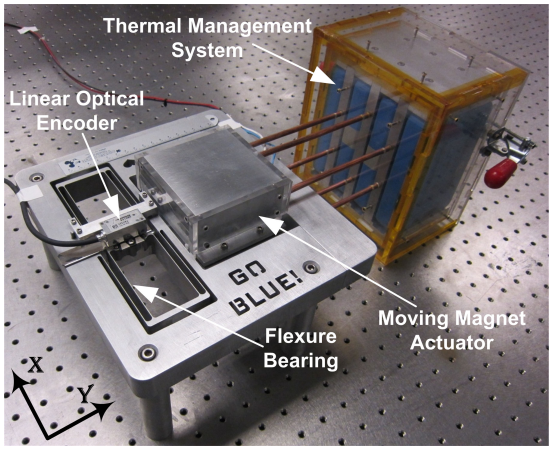

Fig. 11. Single-axis nanopositioning system prototype.

Fig. 10. A removable back plate simplifies the assembly of the MMA with the flexure bearing. Alignment between the MMA, back plate, and flexure bearing is achieved via dowel pins. As shown in Fig. 10 (inset), the motion stage was designed to hold the MMA mover shaft and optical encoder scale (A). The mover shaft is aligned and secured to the motion stage via a sleeve collar (B). Dowel pins (C) provide alignment of the encoder scale with respect to the motion stage. The optical encoder readhead (D) is mounted and aligned using three ground-mounted dowel pins (E). The final, fabricated single-axis nanopositioning system assembly is shown in Fig. 11.

V. Experimental Testing and Results

First, the characteristics of the MMA and TMS were measured, followed by the characterization of the overall motion system. The MMA force was measured using a load cell (Model # ELFF-T4E-20L from Measurement Specialties) in a temporary setup shown in Fig. 12(a). With the magnet held at the nominal position ($\Delta = 0$ mm), the MMA force is plotted with respect to the coil current in Fig. 12(b). The slope of this line provides the measured force constant K_t. This is within 3.5% of the value predicted by FEA; the difference is most likely due to a discrepancy between number of turns employed in the prototype coils and the FEA model. The measured Lorentz force–stroke

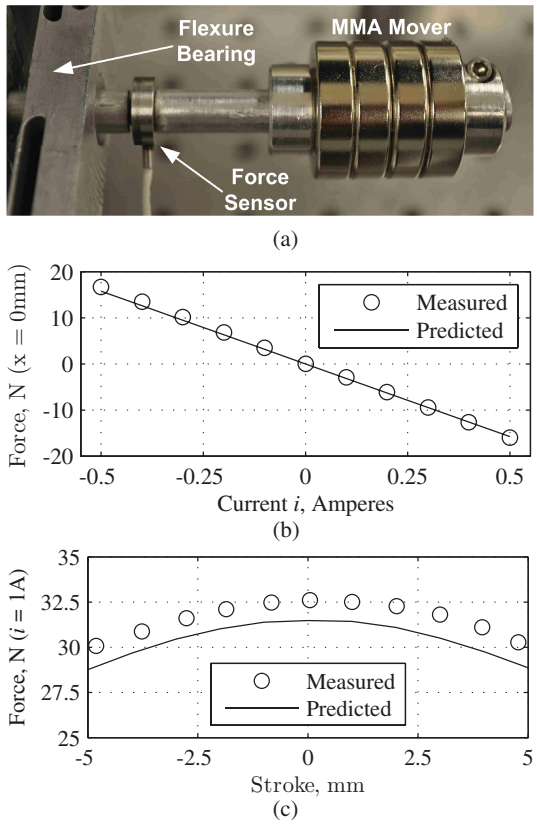

Fig. 12. (a) Setup for MMA force measurement. (b) Measured force constant. (c) Measured force–stroke nonuniformity.

nonuniformity, plotted in Fig. 12(c), is within 10% over the entire ± 5 mm stroke. The constant force offset in this plot is due to the aforementioned discrepancy in K_t.

Fig. 13 shows the measured coil bobbin and motion stage temperatures for an MMA power input of 20 W, with and without the TMS. The motion stage, where the optical encoder is mounted, remains within 0.5 °C of room temperature over the entire testing period, once steady state is reached. This demonstrates the effectiveness of the proposed TMS in maintaining temperature stability.

Next, the open-loop frequency response of the nanopositioning system was measured using a dynamic signal analyzer

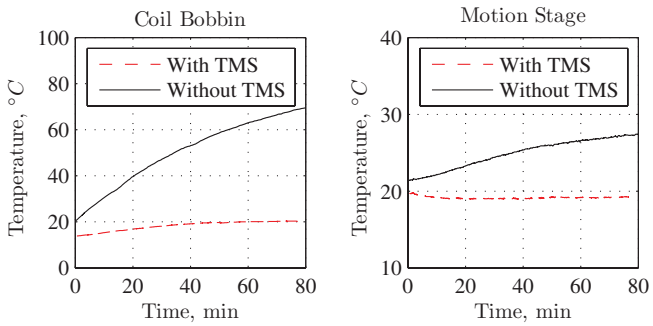

Fig. 13. Temperature rise of the coil bobbin and the motion stage with (- -) and without (—) the TMS.

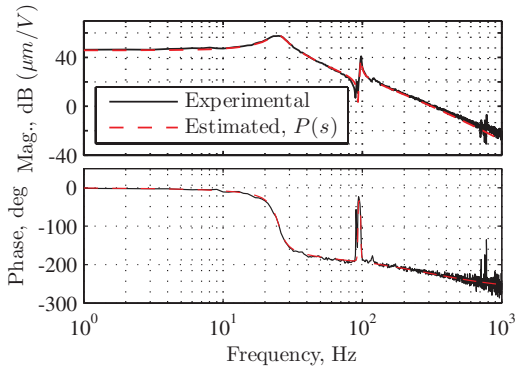

Fig. 14. Open-loop frequency response.

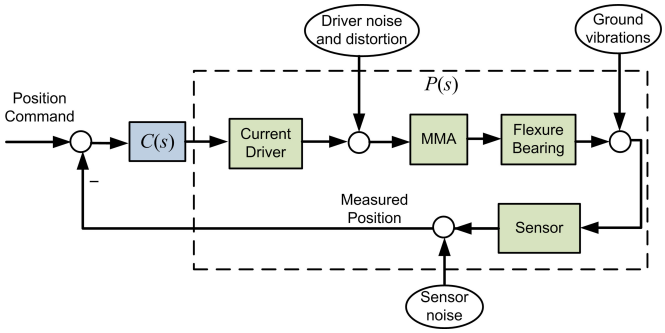

Fig. 15. Feedback architecture.

(SigLab, Model 20-22A). Fig. 14 shows the resulting transfer function between the command to the current driver and the motion stage displacement. As expected, the first natural frequency of the system is found to be 25 Hz. Damping at this resonance peak primarily comes from eddy currents in the aluminum bobbin.

As mentioned earlier, to achieve high speed and high motion quality, the nanopositioning system has to be operated in closed loop (see Fig. 15). This allows attenuation of noise and disturbance from the actuator driver, position sensor, data-acquisition hardware, and ground vibrations, all of which limit the achievable motion quality. Additionally, closed-loop operation enables command tracking over a desired frequency range, by mitigating the effects of harmonic distortion in the current driver and the force–stroke nonuniformity of the MMA. Such command tracking over large motion range is possible as long as the driver and power supply are not saturated.

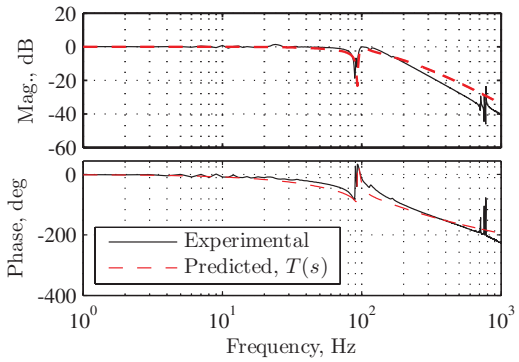

Fig. 16. Closed-loop frequency response.

In order to design a linear feedback controller, a fifth-order transfer function $P(s)$ was fitted to the open-loop frequency response, as shown in Fig. 14. $P(s)$ is given by

$$P(s) = \frac{1.06 \times 10^{10}}{(s+2000)\left(s^2+36.94s+2.46\times 10^4\right)} \times \frac{\left(s^2+4.54s+3.40\times 10^5\right)}{\left(s^2+6.38s+3.76\times 10^5\right)}. \quad (10)$$

This open-loop transfer function is used to design a lag–lead controller $C(s)$ to achieve acceptable closed-loop stability and performance. The lag part includes an integrator and a higher frequency zero to achieve zero steady-state error and the lead part is needed to increase the phase near gain crossover frequency. Upon a few iterations, the following feedback controller was implemented on a real-time hardware from National Instruments (PXI-8106, PXI-6289) at a loop rate of 5 kHz:

$$C(s) = \frac{0.92\left(s^2+37s+2.46\times 10^4\right)}{s\left(s+1\times 10^4\right)}. \quad (11)$$

The frequency response of the resulting closed-loop transfer function

$$T(s) = \frac{P(s)C(s)}{1+P(s)C(s)} \quad (12)$$

along with the experimentally obtained closed-loop frequency response is shown in Fig. 16. The phase margin and gain margin for the loop transfer function are 59° and 21 dB respectively. The small-signal closed-loop bandwidth (−3 dB) of the system is approximately 150 Hz.

The nanopositioning system was tested for point-to-point positioning performance with step commands of 2.5 mm and 20 nm and the measured position response is shown in Fig. 17. In this test, a steady-state positioning error of 20 nm (peak-to-peak) or 4 nm (RMS) was achieved over the entire 10 mm motion range, thus confirming the desired nanometric motion quality and large motion range.

In addition to point-to-point positioning, nanopositioning systems are also employed in scanning-type applications where the motion profile is dynamic in nature, as discussed in Section I. In order to evaluate the dynamic tracking performance, a 3 mm

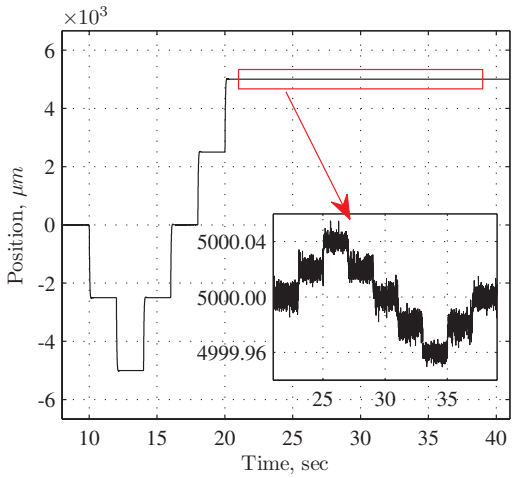

Fig. 17. Motion stage response to 2.5 mm and 20 nm step commands.

TABLE II
MOTION SYSTEM SPECIFICATIONS

Specification	Value	Units
Motion range	10	mm
Open-loop natural frequency	25	Hz
Max. continuous power	20	W
Temperature stability	0.5	°C
Closed-loop resolution	20/4	nm(pp)/nm(RMS)

and 2 Hz sinusoidal signal was applied as the command. The resulting tracking error was observed to be as high as ± 60 μm, which is clearly inadequate in terms of targeted motion quality. This becomes even worse as the command frequency is further increased. This large tracking error is due to the strong higher order harmonics arising from the driver and the actuator nonlinearities [19]. The 25 Hz open-loop bandwidth of the present system proves to be inadequate in suppressing these effects in the closed-loop operation. Planned research tasks to address this are discussed in the next section.

The key engineering specifications of the single-axis nanopositioning system, measured to date, are summarized in Table II.

VI. CONCLUSION

This paper analytically and experimentally establishes the limits of motion performance allowed by MMAs in flexure-based nanopositioning systems. It quantitatively elucidates the various design challenges and tradeoffs that exist in simultaneously achieving range, speed, motion quality, and temperature stability. A new MMA figure of merit, referred to as the dynamic actuator constant, is introduced that captures inherent tradeoffs between the actuator specifications, and limits the performance of the nanopositioning system. The significance of this constant is experimentally validated via the fabrication and testing of a single-axis nanopositioning system. A novel TMS greatly abates the heat dissipation problem associated with MMAs. Promising results for large-range point-to-point nanopositioning are reported. However, dynamic tracking with nanometric motion quality is not attained due to harmonic distortion in the driver, force–stroke nonuniformity of the MMA, and limited natural frequency of the overall system.

This motivates our future work in the design of MMAs that offer greater values of the dynamic actuator constant while maintaining low force–stroke nonuniformity. This includes the conception and optimization of new MMA architectures. Current drivers with even lower harmonic distortion will also be investigated. At the same time, adaptive and learning control methods will be investigated to overcome the nonlinearities and improve the tracking performance for dynamic command profiles.

REFERENCES

[1] S. Verma, K. Won-Jong, and G. Jie, "Six-axis nanopositioning device with precision magnetic levitation technology," *IEEE/ASME Trans. Mechatronics*, vol. 9, no. 2, pp. 384–391, Jun. 2004.
[2] T. Yamada, S. Koganezawa, K. Aruga, and Y. Mizoshita, "A high-performance and low-profile moving-magnet actuator for disk drives," *IEEE Trans. Magn.*, vol. 30, no. 6, pp. 4227–4229, Nov. 1994.
[3] S. Braune and S. Liu, "Design of a novel moving magnet linear motor for use as a valve actuator," in *Proc. 31st Annu. Conf. IEEE Ind. Electron. Soc.*, 2005, pp. 2041–2046.
[4] S. Awtar and G. Parmar, "Physical and control systems design challenges in large range nanopositioning," in *Proc. IFAC Symp. Mechatron. Syst.*, Cambridge, MA, 2010, pp. 153–159.
[5] A. Sinno, P. Ruaux, L. Chassagne, S. Topcu, Y. Alayli, G. Lerondel, S. Blaize, A. Bruyant, and P. Royer, "Enlarged atomic force microscopy scanning scope: Novel sample-holder device with millimeter range," *Rev. Sci. Instrum.*, vol. 78, pp. 1–7, 2007.
[6] Y. K. Yong, B. Bhikkaji, and S. O. Reza Moheimani, "Design, modeling, and FPAA-based control of a high-speed atomic force microscope nanopositioner," *IEEE/ASME Trans. Mechatronics*, [Online]. Available: http://ieeexplore.ieee.org, DOI: 10.1109/TMECH.2012.2194161.
[7] K. Salaita, Y. Wang, and C. A. Mirkin, "Applications of dip-pen nanolithography," *Nat. Nanotechnol.*, vol. 2, pp. 145–155, 2007.
[8] M. van de Moosdijk, E. van den Brink, K. Simon, A. Friz, G. Phillipps, R. Travers, and E. Raaymakers, "Collinearity and stitching performance on an ASML stepper," *Proc. SPIE*, vol. 4688, pp. 858–866, 2002.
[9] W. O'Brien, "Long-range motion with nanometer precision," *Photon. Spectra*, vol. 39, pp. 80–81, Jun. 2005.
[10] J. A. Kramar, "Nanometre resolution metrology with the molecular measuring machine," *Meas. Sci. Technol.*, vol. 16, pp. 2121–2128, 2005.
[11] P. Schellekens, N. Rosielle, H. Vermeulen, M. Vermeulen, S. Wetzels, and W. Pril, "Design for precision: Current status and trends," *CIRP Ann.—Manuf. Technol.*, vol. 47, pp. 557–586, 1998.
[12] J. v. Eijk and T. Ruijl, "Thermal effects in precision engineering (meeting report)," presented at the 7th Eur. Soc. Precision Eng. Nanotechnol. Int. Conf., Bremen, Germany, 2007.
[13] S. Devasia, E. Eleftheriou, and S. O. R. Moheimani, "A survey of control issues in nanopositioning," *IEEE Trans. Control Syst. Technol.*, vol. 15, no. 5, pp. 802–823, Sep. 2007.
[14] M. Kosinskiy, Y. Liu, S. I. U. Ahmed, M. Scherge, and J. A. Schafer, "Tribology of nanopositioning characterization of precision linear bearings on nanometre scale," *VDI Berichte*, issue no. 1950, pp. 215–224, 2006.
[15] C. J. Lin, H. T. Yau, and Y. C. Tian, "Identification and compensation of nonlinear friction characteristics and precision control for a linear motor stage," *IEEE/ASME Trans. Mechatronics*, [Online]. Available: http://ieeexplore.ieee.org, DOI: 10.1109/TMECH.2012.2202679.
[16] G. J. Maeda and K. Sato, "Practical control method for ultra-precision positioning using a ballscrew mechanism," *Precis. Eng.*, vol. 32, pp. 309–318, 2008.
[17] L. Lihua, L. Yingchun, G. Yongfeng, and S. Akira, "Design and testing of a nanometer positioning system," *J. Dyn. Syst., Meas. Control*, vol. 132, pp. 021011-1–021011-6, 2010.
[18] J. Otsuka, T. Tanaka, and I. Masuda, "Development of a sub-nanometer positioning device: Combining a new linear motor with linear motion ball guide ways," *Meas. Sci. Technol.*, vol. 21, p. 037001, 2010.
[19] G. Parmar, D. B. Hiemstra, and S. Awtar, "Large dynamic range nanopositioning using iterative learning control," presented at the ASME Dyn. Syst. Control Conf., Ft. Lauderdale, FL, 2012.
[20] S. T. Smith and R. M. Seugling, "Sensor and actuator considerations for precision, small machines," *Precis. Eng.*, vol. 30, pp. 245–264, 2006.

[21] N. B. Hubbard, M. L. Culpepper, and L. L. Howell, "Actuators for micropositioners and nanopositioners," *Appl. Mech. Rev.*, vol. 59, pp. 324–334, 2006.
[22] J. E. Huber, N. A. Fleck, and M. F. Ashby, "The selection of mechanical actuators based on performance indices," *Proc. R. Soc. Lond. A, Math. Phys. Eng. Sci.*, vol. 453, no. 1965, pp. 2185–2205, 1997.
[23] J.-J. Kim, Y.-M. Choi, D. Ahn, B. Hwang, D.-G. Gweon, and J. Jeong, "A millimeter-range flexure-based nano-positioning stage using a self-guided displacement amplification mechanism," *Mech. Mach. Theory*, vol. 50, pp. 109–120, 2012.
[24] S. C. Woody and S. T. Smith, "Performance comparison and modeling of PZN, PMN, and PZT stacked actuators in a levered flexure mechanism," *Rev. Sci. Instrum.*, vol. 75, pp. 842–848, 2004.
[25] E. Furukawa, M. Mizuno, and T. Doi, "Development of a flexure-hinged translation mechanism driven by two piezoelectric stacks," *JSME Int. J., Series C*, vol. 38, pp. 743–748, 1995.
[26] B. Zhang and Z. Zhu, "Developing a linear piezomotor with nanometer resolution and high stiffness," *IEEE/ASME Trans. Mechatronics*, vol. 2, no. 1, pp. 22–29, Mar. 1997.
[27] K. Uchino, "Piezoelectric ultrasonic motors: Overview," *Smart Mater. Struct.*, vol. 7, pp. 273–285, 1998.
[28] W. Youm, J. Jung, S. Lee, and K. Park, "Control of voice coil motor nanoscanners for an atomic force microscopy system using a loop shaping technique," *Rev. Sci. Instrum.*, vol. 79, pp. 013707-1–013707-6, 2008.
[29] M. Holmes, R. Hocken, and D. Trumper, "The long-range scanning stage: A novel platform for scanned-probe microscopy," *Precis. Eng.*, vol. 24, pp. 191–209, 2000.
[30] T. J. Teo, I. M. Chen, G. Yang, and W. Lin, "A flexure-based electromagnetic linear actuator," *Nanotechnology*, vol. 19, pp. 1–10, 2008.
[31] N. H. Vrijsen, J. W. Jansen, and E. A. Lomonova, "Comparison of linear voice coil and reluctance actuators for high-precision applications," in *Proc. 14th Int. Power Electron. Motion Control Conf.*, Ohrid, Macedonia, 2010, pp. S329–S336.
[32] S. Fukada and K. Nishimura, "Nanometric positioning over a one-millimeter stroke using a flexure guide and electromagnetic linear motor," *Int. J. Precis. Eng. Manuf.*, vol. 8, pp. 49–53, 2007.
[33] B. Yao, C. Hu, Y. Hong, and Q. Wang, "Precision motion control of linear motor drive systems for micro/nano-positioning," in *Proc. Int. Conf. Integr. Commercialization Micro Nanosyst.*, Sanya, Hainan, China, 2007, pp. 1605–1614.
[34] M.-Y. Chen, M.-J. Wang, and L.-C. Fu, "A novel dual-axis repulsive Maglev guiding system with permanent magnet: Modeling and controller design," *IEEE/ASME Trans. Mechatronics*, vol. 8, no. 1, pp. 77–86, Mar. 2003.
[35] M. G. Lee, S. Q. Lee, and D.-G. Gweon, "Analysis of Halbach magnet array and its application to linear motor," *Mechatronics*, vol. 14, pp. 115–128, 2004.
[36] J. de boeij, E. Lomonova, J. L. Duarte, and A. J. A. Vandenput, "Contactless power supply for moving sensors and actuators in high-precision mechatronic systems with long-stroke power transfer capability in x–y plane," *Sensors Actuators A, Phys.*, vol. 148, pp. 319–328, 2008.
[37] J. S. Freudenberg and D. P. Looze, *Frequency Domain Properties of Scalar and Multivariable Feedback Systems*. Berlin, Germany: Springer-Verlag, 1988.
[38] R. E. Clark, D. S. Smith, P. H. Mellor, and D. Howe, "Design optimization of moving-magnet actuators for reciprocating electro-mechanical systems," *IEEE Trans. Magn.*, vol. 31, no. 6, pp. 3746–3748, Nov. 1995.
[39] P. J. Patt, "Frictionless motor material testing," U.S. Patent 6 405 599, Jun. 18, 2002.
[40] H. R. Bolton, "Design aspects of electromagnetic actuators," in *Proc. IEE Colloquium Magn. Mater. Sens. Actuators*, 1994, pp. 1–5.
[41] E. P. Furlani, *Permanent Magnet and Electromechanical Devices*. New York: Academic, 2001.
[42] "Product Model # NCM03-06-005-5JB," H2W Technologies, Santa Clarita, CA, accessed on Feb. 3, 2012.
[43] "Product Model # NCM05-28-180-2LB," H2W Technologies, Santa Clarita, CA, accessed on Feb. 3, 2012.
[44] "Product Model # LA16-19-001A," BEI Kimko Magnetics, Vista, CA, accessed on Feb. 3, 2012.
[45] "Product Model # 6033," Magnetic Innovations, Veldhoven, The Netherlands, accessed on Feb. 3, 2012.
[46] "Application Note 13: Voltage to Current Conversion," Cirrus Logic, Austin, TX, accessed on Feb. 3, 2012.
[47] M. A. Moser, "Shorted turn effects in rotary voice coil actuators," *IEEE Trans. Magn.*, vol. 32, no. 3, pp. 1736–1742, May 1996.
[48] J. M. M. Rovers, J. W. Jansen, J. C. Compter, and E. A. Lomonova, "Analysis method of the dynamic force and torque distribution in the magnet array of a commutated magnetically levitated planar actuator," *IEEE Trans. Ind. Electron.*, vol. 59, no. 5, pp. 2157–2166, May 2012.
[49] D. B. Hiemstra, "Design of moving magnet actuators for flexure based nanopositioning," M.S. thesis, Univ. Michigan, Ann Arbor, MI, 2012.
[50] S. T. Smith, *Flexures: Elements of Elastic Mechanisms*. Amsterdam, The Netherlands: Gordon and Breach, 2000.
[51] S. Awtar, A. H. Slocum, and E. Sevincer, "Characteristics of beam-based flexure modules," *ASME J. Mech. Design*, vol. 129, pp. 625–639, 2007.

David B. Hiemstra received the B.S.E. degree in mechanical engineering with an international minor from the University of Michigan, Ann Arbor, in 2010. He has continued on to pursue graduate studies and research in the Precision Systems Design Laboratory, University of Michigan, focusing on the systematic design and optimization of novel MMAs for large-range, flexure-based nanopositioning systems.

He has been the recipient of the William Mirsky Fellowship, the Rackham Centennial Fellowship, and several other industry-sponsored and academic scholarships. He recently gained additional experience in precision engineering at Kleindiek Nanotechnik, Reutlingen, Germany, as a DAAD RISE Professional Fellow. He currently serves as the President of the Nanotechnology and Integrated Microsystems Student Association at the University of Michigan.

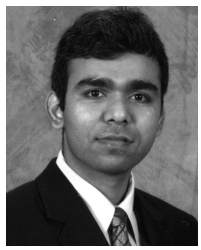

Gaurav Parmar received the B.Tech. degree in mechanical engineering from the Indian Institute of Technology Bombay, Mumbai, India, in 2006. He is currently working toward the Doctoral degree in mechanical engineering at the University of Michigan, Ann Arbor.

He is a Graduate Researcher in the Precision Systems Design Laboratory, University of Michigan. He is a recipient of the Measurement Science and Engineering Fellowship from the National Institute of Science and Technology. His research interests include design and control of ultraprecision motion systems with applications to nanotechnology.

Mr. Parmar received the 2010 ASME Dynamic Systems and Controls Division's best conference paper award in mechatronics. He is a student member of the American Society of Mechanical Engineers.

Shorya Awtar received the B.Tech. degree from the Indian Institute of Technology Kanpur, Kanpur, India, the M.S. degree from Rensselaer Polytechnic Institute, Troy, NY, and the Sc.D. degree from the Massachusetts Institute of Technology, Cambridge, in 1998, 2000, and 2003, respectively, all in mechanical engineering.

He is an Assistant Professor of Mechanical Engineering and the Director of the Precision Systems Design Laboratory, University of Michigan, Ann Arbor. Prior to joining the University of Michigan, he was with the General Electric Co. Global Research Center until 2006. His engineering and research interests include machine design, flexure mechanisms, precision engineering, and mechatronic systems. The current focus of his research group is on precision motion systems for nanometrology and nanomanufacturing, minimally invasive surgical tools, and MEMS actuators and sensors.

Prof. Awtar received the National Science Foundation's CAREER Award in 2009 and the ASME Leonardo da Vinci Award in 2011, among others, for his research and innovations in machine and mechanism design. He is also a member of the American Society of Mechanical Engineers.